

Article

Efficiently Enhancing Electrocatalytic Activity of α -MnO₂ Nanorods/N-Doped Ketjenblack Carbon for Oxygen Reduction Reaction and Oxygen Evolution Reaction Using Facile Regulated Hydrothermal Treatment

Mei Wang, Kui Chen, Jun Liu, Quanguo He, Guangli Li * and Fuzhi Li *

Hunan Key Laboratory of Biomedical Nanomaterials and Devices, College of Life Sciences and Chemistry, Hunan University of Technology, Zhuzhou 412007, China; wangm20140900@126.com (M.W.); chenku201802@163.com (K.C.); junliu@hut.edu.cn (J.L.); hequanguo@126.com (Q.H.)

* Correspondence: guangli010@163.com (G.L.); li-fu-zhi@163.com (F.L.)

Received: 6 March 2018; Accepted: 28 March 2018; Published: 30 March 2018



Abstract: Scalable, low-cost and highly efficient catalysis of oxygen electrocatalytic reactions (ORR/OER) are required for the rapid development of clean and renewable energy conversion/storage technologies. Herein, two types of α -MnO₂ nanorods were prepared under hydrothermal treatment at 150 °C for 0.5 h (MnO₂-150-0.5) or 120 °C for 12 h (MnO₂-120-12), then supported on N-doped ketjenblack carbon (N-KB) as bi-functional ORR/OER catalysts. Their electrocatalytic activities toward ORR and OER were investigated systematically. As a result, MnO₂-150-0.5/N-KB displays superior ORR catalytic activity, with much more positive half-wave potential and much larger limiting current density (0.76 V and 6.0 mA cm⁻²), comparable to those of 20 wt. % Pt/C (0.82 V and 5.10 mA cm⁻²). MnO₂-150-0.5/N-KB also shows high electron transfer number (3.86~3.97) and low yield of peroxides (1~7%) during ORR process in the whole potential range of 0–1.0 V (vs. RHE). Meanwhile, the MnO₂-150-0.5/N-KB also exhibits better OER activity with low overpotential, comparable to IrO₂/N-KB. The excellent electrocatalytic activity of MnO₂-150-0.5/N-KB can be attributed to the synergistic effect, relatively smaller size, higher amount of Mn³⁺, and low charge transfer resistance. This work offers a new strategy for scalable preparation of more efficient and cost-effective α -MnO₂ bi-functional oxygen catalysts.

Keywords: MnO₂ nanorods; electrocatalysis; oxygen reduction reaction; oxygen evolution reaction; hydrothermal treatment

1. Introduction

Efficient catalysts for oxygen electrocatalytic reactions (ORR/OER) are required for the rapid development of clean and renewable energy conversion/storage systems, including fuel cells and metal/air batteries. As is well known, precious metals and their alloys are considered to be the most efficient commercial ORR catalysts while ruthenium and iridium oxides are still the most commonly used OER catalysts [1,2]. However, their high cost and rarity have become the major hurdles in large-scale commercial application [3]. Hence, it is necessary to develop cost-effective and highly efficient alternative electrocatalysts for ORR and OER.

Recently, much effort has been devoted to developing non-noble metal catalysts as promising candidates to substitute noble metal catalysts (i.e., platinum-based catalysts). Various non-noble materials have been developed for ORR or OER [4–8], including but not limited to carbon, polymer,

and transition metal oxides like MnO_2 , Fe_3O_4 and Co_2O_3 . Among them, manganese oxides (MnO_x) have received increasing attention due to their abundance, low cost, environment friendliness, variable valence and high catalytic activity towards ORR and OER [9–14]. Until now, various MnO_2 -based electrocatalysts have been developed for ORR [15–17] and OER [16,18–20].

To pursue superior catalytic activity, the influence factors of MnO_2 on the ORR/OER activity have been extensively investigated. First, the electrocatalytic activities of MnO_2 nanostructures are highly related to their crystalline phase. It was reported that the catalytic performance of nano- MnO_2 increased in order of β - < λ - < γ - < α - \approx δ - MnO_2 [21,22]. Numerous reports confirmed the α - MnO_2 possess high catalytic activity for ORR [15,16,23,24] and OER [16,19], owing to the edge and corner shared $[\text{MnO}_6]$ octahedral forming a 2×2 tunnel structure with charge-balancing ions. The improved OER electrocatalytic performance of α - MnO_2 is mainly due to its abundant di- μ -oxo bridges [10]. Secondly, the ORR electrocatalytic performance of nano- MnO_2 strongly depends on its morphologies. Cheng and coworkers investigated systematically the effect of the particle size and morphology of nano- MnO_2 -based catalyst on ORR activity [15]. The results demonstrate that nanostructure α - MnO_2 is superior to counterpart microstructures with higher oxygen reduction potential and larger current density [15]. The ORR activity increases when particle size decreases because of large surface area and numerous surface defects [10]. Moreover, 1-dimensional α - MnO_2 nanowires exhibit better catalytic performance than 3-dimensional α - MnO_2 nanospheres with similar surface area [10]. In another report, α - MnO_2 nanorods/nanotubes also show higher ORR activity compared to the core-corona spheres δ - MnO_2 [24]. Finally, the electrocatalytic activity is also affected by the amount of Mn^{3+} in MnO_2 . It is believed that Mn^{3+} is favorable for ORR [25] and OER [26] because of single e_g occupation. Therefore, much attention has been paid to increasing the content of Mn^{3+} . For example, heat treatment is proved to be an effective way to increase the amount of Mn^{3+} because heat treatment in Ar and Air can cause oxygen nonstoichiometry [27]. It was also reported that hydrogenation [28] and cations doping [29,30] also increase the amount of Mn^{3+} in MnO_2 . Furthermore, the amount of Mn^{3+} can be tuned by adjusting the synthesis procedure appropriately. Generally, the preparation of MnO_2 is either by the oxidation of Mn^{2+} , or by the reduction of Mn^{7+} . Chen et al. compared nano- MnO_2 prepared by three types of potassium salt oxidants with different reduction potentials, and confirmed that the reaction rate is directly dependent on the redox potential of oxidant or reductant used [31]. Inspired by Chen's work, two types of α - MnO_2 (namely dandelion-like and urchin-like) were prepared by two redox reactions with different redox potential, and the ORR/OER activities were compared systemically [32]. The results demonstrated that dandelion-like MnO_2 was of higher electrocatalytic performance than the urchinlike one, attributing to its relatively larger BET and electrochemical active surface area, higher ratio of $\text{Mn}^{3+}/\text{Mn}^{4+}$, and low charge transfer resistance [32].

Activated by the above findings, we proposed a facile regulated hydrothermal method to prepared α - MnO_2 nanorods (α - MnO_2 NRs) of small particle size and high content Mn^{3+} , aiming to improve the ORR/OER activity. The α - MnO_2 NRs were prepared from the oxidation of a MnSO_4 precursor by KMnO_4 during various hydrothermal reaction temperatures and times. It is believed that the fast reaction rate could increase disorder and produce defects with more Mn^{3+} in MnO_2 . Based on this, we hypothesize that raising the temperature and shortening the reaction time will lead to greater increase defects and Mn^{3+} . To further improve the ORR/OER, N-doped ketjenblack carbon (N-KB) was used as catalyst support to construct α - MnO_2 NRs/N-KB bi-functional oxygen catalysts. As expected, MnO_2 -150-0.5 (hydrothermal treatment at 150 °C for 0.5 h) /N-KB exhibits much better ORR/OER activity than that of MnO_2 -120-12 (hydrothermal treatment at 120 °C for 12 h) /N-KB due to its smaller size has higher $\text{Mn}^{3+}/\text{Mn}^{4+}$ ratio. This work offers a new strategy on scalable preparation of more efficient and cost-effective α - MnO_2 bi-functional oxygen catalysts for ORR/OER.

2. Results and Discussion

2.1. Morphological Characterization

The surface morphologies of as-prepared MnO₂ NR samples were characterized by scanning electron microscope (SEM). The SEM images of MnO₂-150-0.5 (a, b, and c) and MnO₂-120-12 (d, e, and f) are shown in Figure 1. The surface morphologies of MnO₂ NRs prepared with various hydrothermal treatment temperature as well as time is quite different. Irregular rhombic morphology consisting of uniform nanorod-like structures are observed on the MnO₂-150-0.5. In contrast, the MnO₂-120-12 samples possess typical amorphous structures. Moreover, the average diameters of MnO₂-150-0.5 and MnO₂-120-12 are 17 nm and 33 nm approximately. Obviously, MnO₂-150-0.5 has smaller size than those of MnO₂-120-12. It is believed that higher reacting temperature causes the faster reaction rate, and the faster reaction rate causes more Mn³⁺ content in MnO₂ (seen in Table 1). In addition, the shorter reacting time gives less chance for particles to aggregate, leading to smaller particle size. The decrease in the particle size to the nanometer scale can increase the surface-to-volume ratio. As result, the MnO₂-150-0.5 has much larger specific surface area, which will provide more catalytic activity sites and energetically facilitate the electrocatalytic activity for ORR/OER.

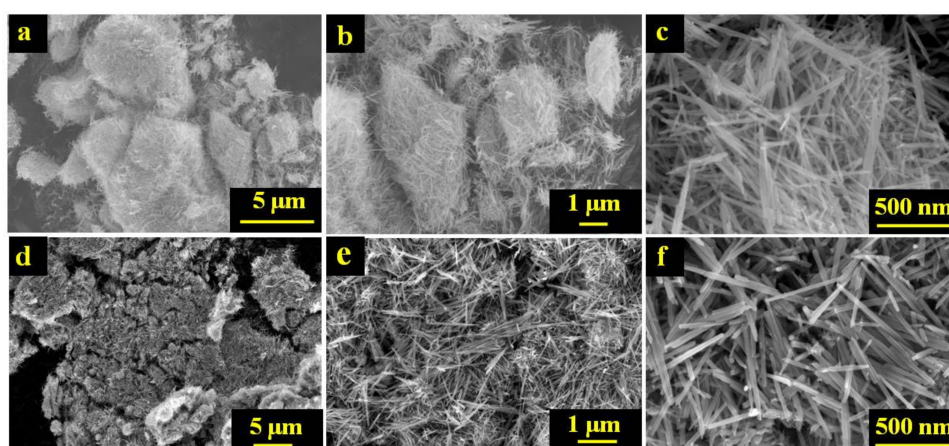


Figure 1. SEM images of MnO₂-150-0.5 (a–c) and MnO₂-120-12 (d–f) at various resolutions.

Table 1. Ratios of Mn³⁺/Mn⁴⁺ in MnO₂-150-0.5 and MnO₂-120-12 from the X-ray photoelectron spectroscopy (XPS) results.

Samples	Peaks	Ion Species	Peak Position (eV)	Peak Area	Mn ³⁺ /Mn ⁴⁺
MnO ₂ -150-0.5	2P _{3/2}	Mn ³⁺	642.35	51,009.41	2.16
		Mn ⁴⁺	643.70	25,816.35	
	2P _{1/2}	Mn ³⁺	653.95	30,811.95	
		Mn ⁴⁺	655.30	12,019.14	
MnO ₂ -120-12	2P _{3/2}	Mn ³⁺	642.35	41,672.21	1.96
		Mn ⁴⁺	643.70	23,236.07	
	2P _{1/2}	Mn ³⁺	653.95	25,282.41	
		Mn ⁴⁺	655.30	10,952.38	

The detained microstructure of MnO₂-150-0.5 was further characterized by transmission electron microscopy (TEM) and high resolution transmission electron microscopy (HRTEM) (Figure 2). As shown in Figure 2a,b, the typical nanorod-like structure is presented on the MnO₂-150-0.5 with an average diameter of ca. 20 nm, which is in accordance with the SEM results. In Figure 2c,d, the distances between adjacent lattice fringes are 0.694 nm and 0.491 nm, attributed to (1 1 0) and (2 0 0) planes of α-MnO₂ NRs respectively.

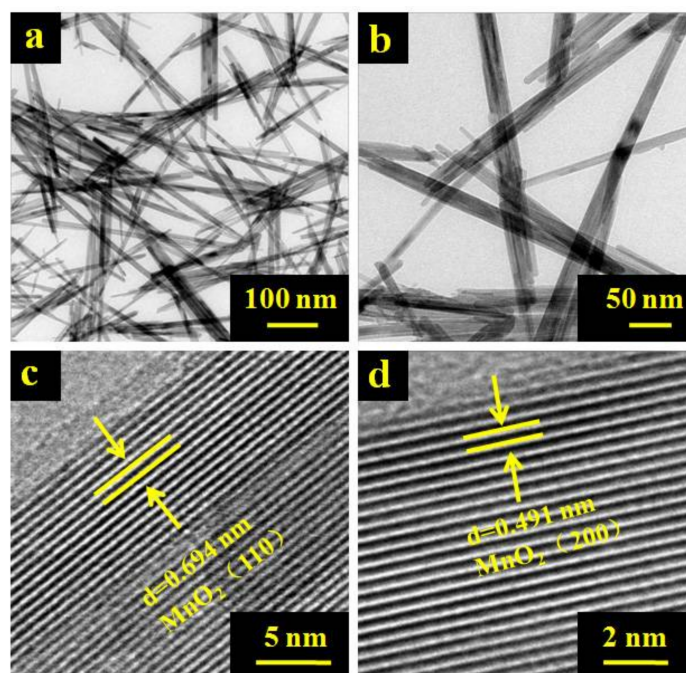


Figure 2. TEM (a,b) and HRTEM images (c,d) of MnO₂-150-0.5 at different resolutions.

2.2. X-ray Diffraction (XRD) Pattern

The crystal phases of MnO₂-150-0.5 and MnO₂-120-12 are determined using XRD (Figure 3). These two samples provide sharp and narrow peaks suggesting they are crystalline. Furthermore, the diffraction peaks of these two samples are clearly indexed into the pure tetragonal phase of α -MnO₂ (JCPDS card PDF file no. 44-0141) [32]. No other peaks are observed in the XRD patterns, demonstrating high purity and crystallinity of these two samples. The nearly identical XRD patterns confirmed that the difference in ORR activity is not because of different crystalline phase existence.

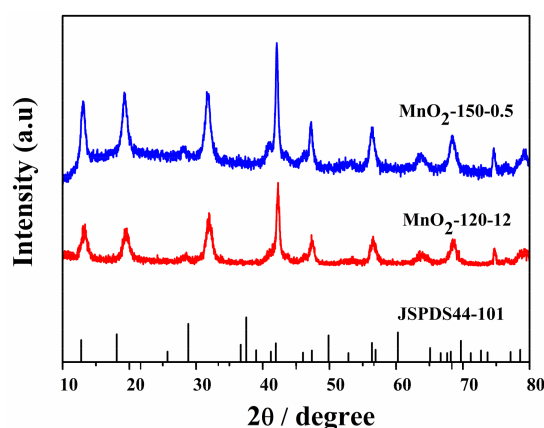


Figure 3. XRD patterns of MnO₂-150-0.5 and MnO₂-120-12.

2.3. XPS Analysis

XPS technique was employed to identify the elemental compositions and valence states of two samples, and the results are shown in Figure 4. The XPS spectra of Mn *2p* both in MnO₂-150-0.5 (Figure 4a) and MnO₂-120-12 (Figure 4b) can be fitted into four peaks at 642.35 eV, 643.70 eV, 653.95 eV and 655.30 eV, which are assigned to Mn³⁺ (*2p*_{3/2}), Mn⁴⁺ (*2p*_{3/2}), Mn³⁺ (*2p*_{1/2}), Mn⁴⁺ (*2p*_{1/2}) species, respectively [2,14,32,33]. As listed in Table 1, the total value of Mn³⁺/Mn⁴⁺ for MnO₂-150-0.5 is

2.16, and the one in MnO₂-120-12 is 1.96, indicating that more Mn³⁺ is existing in the MnO₂-150-0.5 sample than in the MnO₂-120-12 sample. It also means there are more surface crystalline defects in MnO₂-150-0.5 than MnO₂-120-12 [19]. The higher Mn³⁺ content in MnO₂-150-0.5 sample should be ascribed to the more disorders and surface defects produced by raising of hydrothermal treatment temperature and shortening hydrothermal treatment. It is believed that higher Mn³⁺ content in MnO₂ can lead to better electro-catalytic performance, due to the single electron occupation in σ^* -orbital (e_g) of Mn³⁺ [12,26,32].

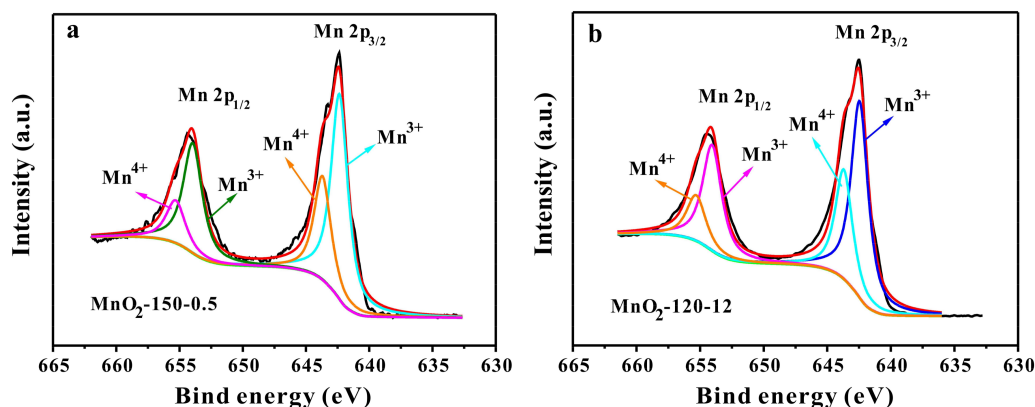


Figure 4. Mn 2p XPS spectra of MnO₂-150-0.5 (a) and MnO₂-120-12 (b).

2.4. ORR Catalytic Activities

To compare the ORR catalytic activities of the as-prepared two samples, linear sweep voltammetry (LSV) curves were recorded at a rotating rate of 1600 rpm (Figure 5). As can be seen, MnO₂-150-0.5/N-KB exhibits slightly better ORR catalytic activity compared to that of MnO₂-120-12/N-KB, with more positive half-wave potential and relative higher limiting current. It can be explained by the facts that MnO₂-150-0.5 have higher amount of Mn³⁺ and smaller particle sizes. Owing to the single electron occupation in σ^* -orbital (e_g), the Mn³⁺ are found to be favors for ORR and OER in previous reports [26]. Hence, more content of Mn³⁺ in MnO₂, better electro-catalytic performance [32]. On the other hand, small particle size tends to have large electrochemical active surface area, which also enhance the electrocatalytic activity. Hereafter, the oxygen electrocatalytic activities for MnO₂-150-0.5 was further investigated.

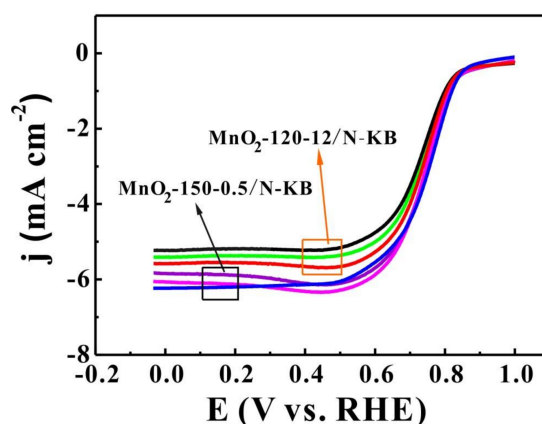


Figure 5. LSV curves of MnO₂-150-0.5/N-KB and MnO₂-120-12/N-KB on rotating disk electrode (RDE) were recorded in O₂-saturated 0.1 M KOH solution at a scan rate of 10 mV·s⁻¹ with a rotation rate of 1600 rpm ($n = 3$).

The LSV curves for KB, N-KB, MnO₂-150-0.5, MnO₂-150-0.5/N-KB and 20% Pt/C in O₂-saturated 0.1 M KOH solution at rotating rate of 1600 rpm are presented in Figure 6a. For comparison, LSV curves of these catalysts in Ar-saturated 0.1 M KOH solution were also measured as their baselines (Figure 7). Obviously, ORR hardly occurs in Ar-saturated 0.1 M KOH solution. As a result, there is no apparent electrochemical responses in Ar-saturated 0.1 M KOH solution. In contrast, pronounced electrochemical responses occur in O₂-saturated 0.1 M KOH solution due to the presence of ORR.

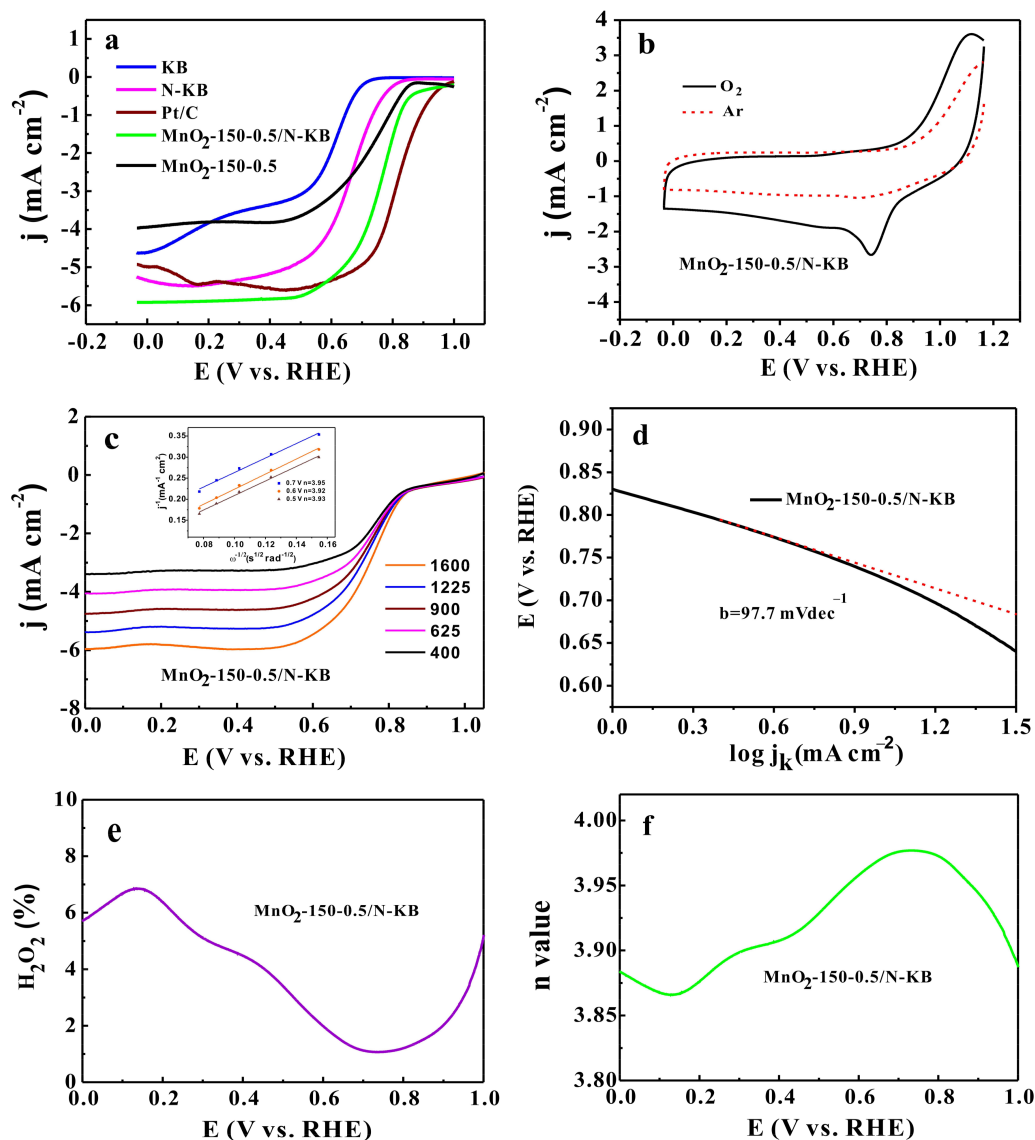


Figure 6. (a) LSV curves of KB, N-KB, pure MnO₂-150-0.5, MnO₂-150-0.5/N-KB and 20 wt. % Pt/C on RDE in O₂-saturated 0.1 M KOH solution at a scan rate of 10 mV·s⁻¹ with a rotation rate of 1600 rpm; (b) CV curves of MnO₂-150-0.5/N-KB in O₂-saturated (black solid line) and Ar-saturated (red dotted line) 0.1 M KOH solution; (c) LSV curves of MnO₂-150-0.5/N-KB at different rotating rate in O₂-saturated 0.1 M KOH solution at a scan rate of 10 mV·s⁻¹ and K-L plots for MnO₂-150-0.5/N-KB (inset); (d) Tafel plots of kinetic current for MnO₂-150-0.5/N-KB; (e) electron transferred number (*n*) of MnO₂-150-0.5/N-KB; (f) Percentage of peroxide yields (H₂O₂%) of MnO₂-150-0.5 /N-KB.

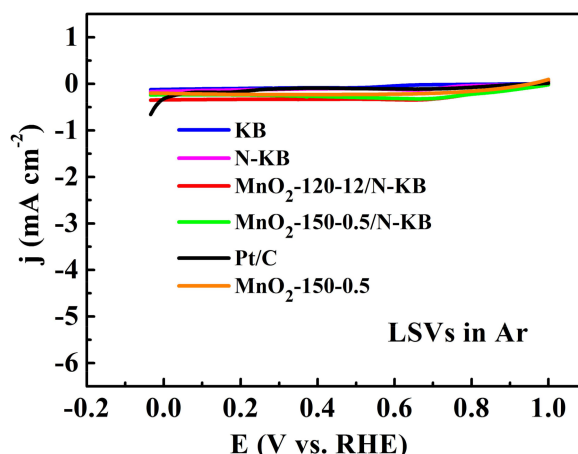


Figure 7. LSV curves of various catalysts on RDE were recorded in Ar-saturated 0.1 M KOH solution at a scan rate of $10 \text{ mV}\cdot\text{s}^{-1}$ with a rotation rate of 1600 rpm.

Evidently, KB samples show very poor ORR activity, with low negative half-wave potential and current density. After doping nitrogen into KB, N-KB catalytic exhibits much better ORR activity, which is most probably due to the more catalytic active sites for N-doped samples [34]. Pure MnO_2 -150-0.5 also shows poor ORR activity, which is due to its poor electric conductivity. As expected, MnO_2 -150-0.5/N-KB displays the superior ORR catalytic activity, with much more positive half-wave potential and much higher limiting current density (0.76 V and $6.0 \text{ mA}\cdot\text{cm}^{-2}$), comparable to that of Pt/C (0.82 V and $5.10 \text{ mA}\cdot\text{cm}^{-2}$). This phenomenon can be explained by the following reasons. Firstly, the superior ORR activity is mainly due the synergistic effect between α - MnO_2 nanorods and N-KB. The MnO_2 /KB materials not only have the inherited advantages from the component materials (excellent catalytic performance for MnO_2 nanorods and high electric conductivity for N-KB), but also improve ORR activity due to synergetic effect. Moreover, the presence of intrinsically abundant di- μ -oxo bridges in α - MnO_2 nanorods greatly accelerate the ORR [9,12,16,32,35]. Finally, its small particle sizes and high content of Mn^{3+} species in its inner matrix also contributed [12,26,32,36].

Figure 6b shows CV curves of MnO_2 -150-0.5/N-KB in O_2 -saturated (black solid line) and Ar-saturated (red dotted line) 0.1 M KOH solution. There is no visible OPR peak when the electrolyte is saturated with Ar. In contrast, well-defined ORR peak is observed in the O_2 -saturated 0.1 M KOH solution, demonstrating the excellent electrocatalytic activity for ORR. More interestingly, all CV curves (both Ar and O_2 saturated) appear strong $\text{Mn}^{3+}/\text{Mn}^{4+}$ redox peaks [32,37] in the potential range of 0.96 to 1.16V. This phenomenon agrees well with previous reports [32,38]. The α - MnO_2 nanorods underwent a reduction from Mn^{4+} to Mn^{3+} in the surfaces of solid phase before the ORR process. Then, the Mn^{3+} had its one σ^* electron transferred to O-O π^* orbital and converted back into Mn^{4+} [32]. Therefore, higher Mn^{3+} content results in more available adsorption sites for O_2 , which eventually improves the electrocatalytic activity for ORR [26,29,32,38].

The LSV curves of MnO_2 -150-0.5/N-KB at different rotating rates were also measured to assess the kinetics of ORR. As shown in Figure 6c, the limiting current densities increase with the raising of the rotating rates, attributing to minimize the concentration polarization due to the shortened diffusion distance at high rotating rates [39]. The curves inserted in Figure 6c exhibits the Koutechy-Levich (K-L) plots obtained from these LSV curves from 400 to 1600 rpm. The K-L plots are almost parallel with each other, suggesting similar electron transfer numbers for ORR at various potentials [40]. The electron transferred numbers (n) are further calculated from the slope of the K-L plots. The n is around 3.95, which suggests MnO_2 -150-0.5/N-KB favors a 4e transfer oxygen reduction mechanism [39,40].

The ORR kinetics was further assessed by Tafel slope (b), electron transfer number (n) and peroxide yields ($\text{H}_2\text{O}_2\%$). As depicted in Figure 6d, the Tafel slope of MnO_2 -150-0.5/N-KB is 97.7 mV

per decade, which is close to the one of Pt/C (~82 mV per decade) in the reference obtained at the same experimental condition [34]. This suggests MnO₂-150-0.5/N-KB has similar kinetic behavior with the commercial catalyst 20 wt. % Pt/C. To further verify the ORR mechanism, the rotating-ring-disk electrode (RRDE) technique was performed to measure electron transfer number (*n*) and peroxide yields (H₂O₂%). As illustrated in Figure 6e, the *n* values of MnO₂-150-0.5/N-KB (~3.86 to 3.97) are close to 4.0 in the whole potential range of 0~1.0 V (vs. RHE), further confirming 4e transfer oxygen reduction mechanism for MnO₂-150-0.5/N-KB. It is noteworthy that the baseline has been subtracted to avoid overestimate the electron transfer number. Moreover, the percentage of peroxide yields (H₂O₂%) during the oxygen reduction is very low (about 1~7%) in the potential range of 0~1.0 V (vs. RHE). All these findings confirm a 4e oxygen reduction mechanism for ORR.

To further investigate the role of ion and charge transfer in the ORR, EIS of MnO₂-150-0.5/N-KB and MnO₂-120-12/N-KB were recorded in O₂-saturated 0.1 M KOH solution at 0.165 V (vs. RHE). The Nyquist plots are shown in Figure 8, in which the EIS data have been fitted according to the equivalent circuit (inset of Figure 8). The equivalent circuit consists of R_s, R_f, R_{ct}, C and W_o represents uncompensated solution resistance, intrinsic resistance of the catalyst, charge transfer resistance, capacitance of double layer and Warburg impedance (relating to diffusion impedance) respectively. As listed in Table 2, the charge transfer resistance (R_{ct}) of these two samples comparable (49.47 Ω and 48.32 Ω respectively). The effect of R_{ct} on the ORR activities is almost same for these two samples. Besides, the catalytic performance of nano-MnO₂ increased in order of β- < λ- < γ- < α- ≈ δ-MnO₂ [21,22]. In a previous report, α-MnO₂ nanorods/nanotubes also show higher ORR activity compared to the core-corona spheres δ-MnO₂ [24]. It is believed that the α-MnO₂ nanorods-based bifunctional catalysts have high ORR activity. For these reasons, the ORR activity of MnO₂-150-0.5/N-KB is a little higher than that of MnO₂-120-12/N-KB (Figure 5). The difference between MnO₂-120-12/N-KB and MnO₂-150-0.5/N-KB only arises from the particle size and Mn^{3+/4+} ratio.

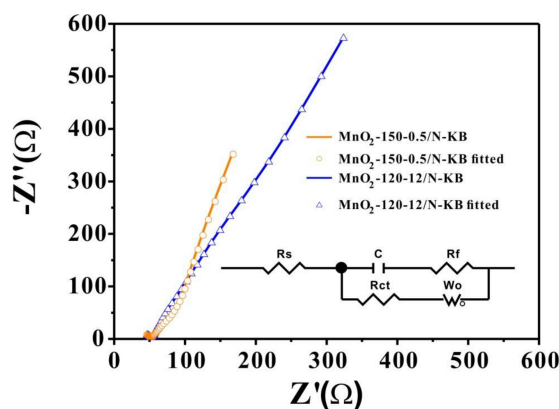


Figure 8. Nyquist plots of MnO₂-150-0.5/N-KB and MnO₂-120-12/N-KB obtained from EIS measurements in O₂-saturated 0.1 M KOH solution at 0.165 V (vs. RHE) and the inserted is the corresponding equivalent circuit.

Table 2. Component values of the fitted equivalent circuit based on the ORR Nyquist plots.

Samples	R _s (Ω)	R _f (Ω)	R _{ct} (Ω)	C (F)	W _o -R	W _o -T	W _o -P
MnO ₂ -150-0.5/N-KB	49.47	5.3	68.0	0.00108	10.94	0.01586	0.40993
MnO ₂ -120-12/N-KB	48.32	7.2	72.2	0.00067	33.00	0.01125	0.32217

2.5. OER Activities

To further compare their electrocatalytic performances, OER activities of the two as-prepared samples (namely MnO₂-150-0.5/N-KB and MnO₂-120-12/N-KB) were tested by RDE experiments

at a scan rate of $10 \text{ mV}\cdot\text{s}^{-1}$. Generally, OER activities are judged by the potential at the current density of $10 \text{ mA}\cdot\text{cm}^{-2}$. As illustrated in Figure 9, $\text{MnO}_2\text{-150-0.5/N-KB}$ (1.83 V) is shift 110 mV more negative than $\text{MnO}_2\text{-120-12/N-KB}$ (1.94 V), which means the $\text{MnO}_2\text{-150-0.5/N-KB}$ catalyze OER at lower overpotential than $\text{MnO}_2\text{-120-12/N-KB}$ sample. In other words, the $\text{MnO}_2\text{-150-0.5/N-KB}$ exhibits much better OER kinetic behavior than $\text{MnO}_2\text{-120-12/N-KB}$. Moreover, the overpotential of $\text{MnO}_2\text{-150-0.5/N-KB}$ is close to the standard catalyst $\text{IrO}_2\text{/N-KB}$ with the same loading of catalysts. Similar to the ORR, the higher Mn^{3+} content [26] and smaller size of $\alpha\text{-MnO}_2$ nanorods also plays a vital role on the OER.

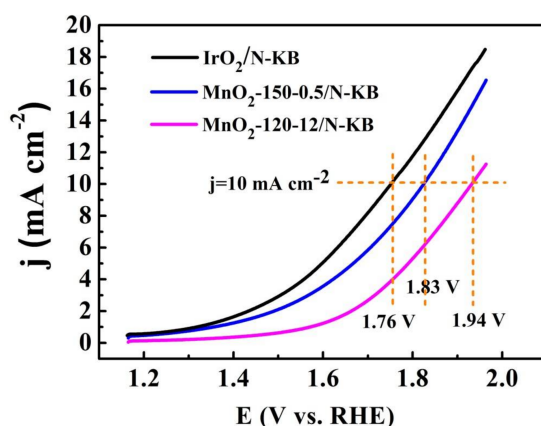


Figure 9. OER performances of $\text{MnO}_2\text{-150-0.5/N-KB}$, $\text{MnO}_2\text{-120-12/N-KB}$ and $\text{IrO}_2\text{/N-KB}$ evaluated by LSVs in 0.1 M KOH solution at a scan rate of $10 \text{ mV}\cdot\text{s}^{-1}$ with a rotation speed of 1600 rpm.

The ionic and charge transfer play an important role in OER [10]. Thus, the electrochemical impedance spectroscopy (EIS) was recorded to give deep insights into the OER process. The Nyquist plots are shown in Figure 10, in which the EIS data have been fitted according to the equivalent circuit (inset of Figure 10). The equivalent circuit consists of R_s , R_f , R_{ct} , C and CPE represents uncompensated solution resistance, intrinsic resistance of the catalyst, charge transfer resistance, capacitance of catalyst and constant phase element of double layer, respectively. All the fitting parameters are listed in Table 3. The R_s relating to the uncompensated solution of these two samples is comparable (59.13Ω and 61.35Ω , respectively). The R_{ct} relates to the reaction kinetics, $\text{MnO}_2\text{-150-0.5/N-KB}$ exhibits lower charge transfer resistance (227.7Ω) than that of $\text{MnO}_2\text{-120-12/N-KB}$ (310.2Ω). Note it is in good accordance with the OER performance.

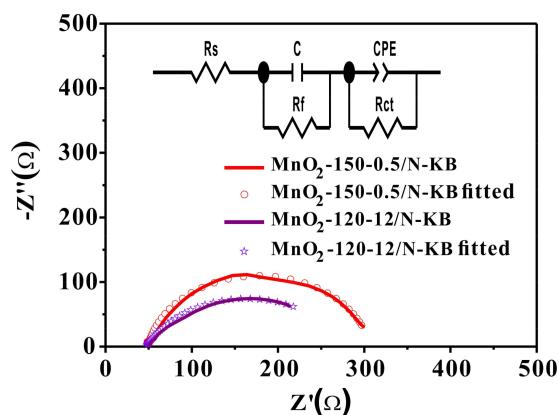


Figure 10. Nyquist plots of $\text{MnO}_2\text{-150-0.5/N-KB}$ and $\text{MnO}_2\text{-120-12/N-KB}$ obtained from EIS measurements in O_2 -saturated 0.1 M KOH solution at 1.665 V (vs. RHE) and the inserted is the corresponding equivalent circuit.

Table 3. Component values of the fitted equivalent circuit based on the Nyquist plots.

Samples	R_s (Ω)	R_f (Ω)	R_{ct} (Ω)	C (F)	CPE-T	CPE-P
MnO ₂ -150-0.5/N-KB	59.13	5.12	227.7	0.05920	0.002868	0.712
MnO ₂ -120-12/N-KB	61.39	9.21	310.2	0.05640	0.001926	0.889

2.6. Durability of Electrocatalysts

The electrocatalytic durability is a major concern in practical applications. The stability of MnO₂-150-0.5 and MnO₂-120-12 for ORR was evaluated by the half-wave potential decay ($\Delta E_{1/2}$) before and after the accelerated durability test (ADT). The ADT was performed by subjecting catalyst to 5000 cycles from 0 to 1.0 (vs. RHE) in O₂-saturated 0.1 M KOH solution at room temperature with a scan rate of 100 mV s⁻¹. As shown in Figure 11a, the half-wave potential of MnO₂-150-0.5/N-KB exhibits a negative shift of ~37 mV after 5000 cycles, a little larger than that of 20% Pt/C (Figure 11c, ~22 mV) and less than that of MnO₂-120-12/N-KB (Figure 11b, ~49 mV). The results reveal that the durability of MnO₂-150-0.5/N-KB is better than that of MnO₂-120-12/N-KB. However, the durability of MnO₂-150-0.5/N-KB still need to be improved.

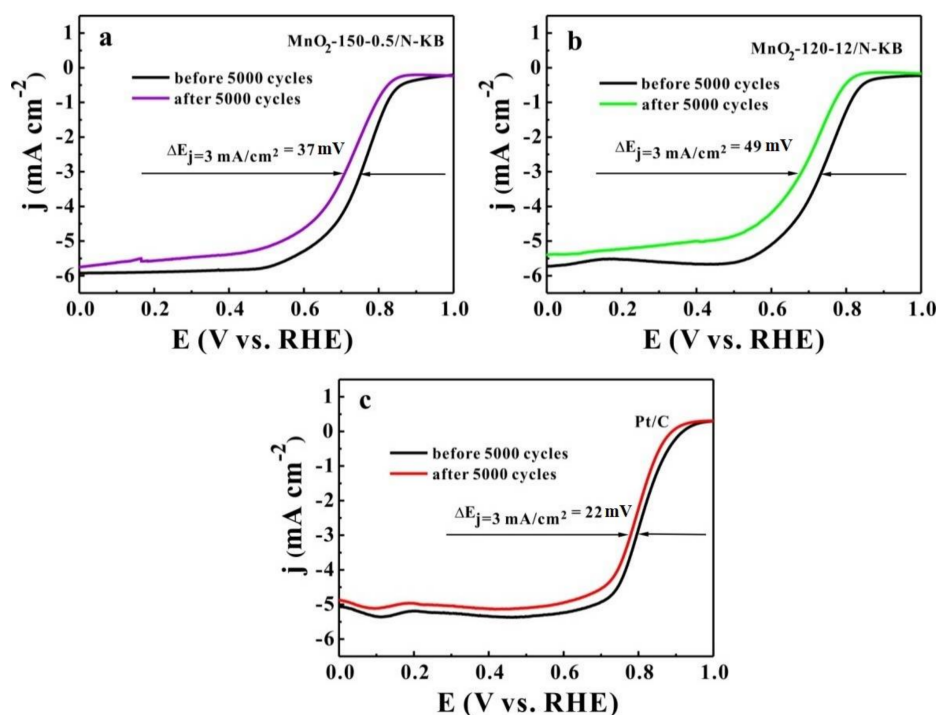


Figure 11. LSV curves of MnO₂-150-0.5 (a), MnO₂-120-12 (b) and Pt/C (c) before and after the accelerated durability test (ADT). The ADT was performed by subjecting catalyst to 5000 circles from 0.57 to 0.82 V (vs. RHE) in O₂-saturated 0.1 M KOH solution at room temperature at a scan rate of 100 mV s⁻¹. The baselines had been subtracted.

3. Experiment

3.1. Chemical and Solutions

Concentrated hydrochloric acid (HCl, 37%), manganese sulfate monohydrate (MnSO₄·H₂O), potassium permanganate (KMnO₄), melamine and ethanol were purchased from Sigma Aldrich Ltd. (St. Louis, MO, USA, <http://www.sigmaaldrich.com>). Ketjenblack carbon (EC-600J) was chosen as carbon support material, which was supplied by AkzoNobel (Amsterdam, The Netherlands). All reagents were of analytical grade and used directly without any further purification.

3.2. Preparation of α -MnO₂ Nanorods

The α -MnO₂ nanorods (α -MnO₂ NRs) were prepared from the oxidation of a MnSO₄ precursor by KMnO₄ during hydrothermal treatment. Typically, 2.03 g of manganese sulfate monohydrate (MnSO₄·H₂O) and 1.26 g of potassium permanganate (KMnO₄) were added into 80 mL of deionized water and agitated 5 min to form a homogenous aqueous solution. Then, 4 mL concentrated hydrochloric acid (37%) was added into the above solution under vigorous agitating for 5 min. The resulting solution was transferred to a 100 mL Teflon-lined stainless steel autoclave, then hydrothermal treated at 150 °C for 30 min or 120 °C for 12 h. Afterwards the autoclave was taken out and naturally cooled to room temperature. Finally, the as-obtained product was vacuum filtrated with a 0.15 μ m pore sized filter membrane, then dried overnight at 80 °C for further use. The obtained samples are denoted in the format: MnO₂-hydrothermal treatment temperature-hydrothermal treatment time. For example, MnO₂-150-0.5 denotes a sample prepared by hydrothermal treatment at 150 °C for 0.5 h.

3.3. Preparation of N-Doped Ketjenblack Carbon

To begin, 0.2 g of ketjenblack carbon (KB) and 1.2 g of melamine were dispersed in 80 mL deionized water under ultrasonication for 30 min. Then, the resulting solution was sealed into a 100 mL Teflon-lined stainless steel autoclave and heated at 120 °C for 24 h. After it was cooled down to room temperature naturally, the as-obtained product was vacuum filtrated using a filter membrane of 0.15 μ m pore size and dried overnight at 80 °C. After carefully ground by agate mortar for more than 10 min, the resulting powder was transferred to a piece of porcelain boat, which was then covered with another piece of porcelain boat and further wrapped by copper foil. The treated porcelain boat was placed into a tube furnace and then heated to 650 °C for 2 h at a heating rate of 5 °C min⁻¹ in argon flow. After that, it was naturally cooled down to room temperature, and hereafter the as-prepared samples were denoted as N-KB.

3.4. Physical Characterization of Catalysts

The morphologies and microstructures of as-prepared catalysts were characterized using TEM (Titan G2 60-300, FEI, Hillsboro, OR, USA) and SEM (FIB 600i, FEI, Hillsboro, OR, USA). The crystallographic phase and structure of MnO₂ NRs were investigated by XRD. The XRD patterns were recorded on X-ray diffractometer (Rigaku D/Max 2550, Tokyo, Japan) with Cu-K α radiation ($\lambda = 1.5406 \text{ \AA}$). XPS was measured on K-Alpha1063 spectrometer (Thermo Scientific Co., Waltham, MA, USA) using a monochromated aluminum anode X-ray source with K α radiation (12 kV, 6 mA).

3.5. Electrochemical Measurements

The electrochemical experiments were performed on CHI760E electrochemical workstation (Shanghai Chenhua Inc., Shanghai, China) using three-electrode assemble in O₂-saturated 0.1 M KOH. Double fluid boundary Ag/AgCl electrode and platinum wire worked as the reference electrode and auxiliary electrode, separately. The work electrodes prepared according to the following procedures. 2 mg of as-prepared α -MnO₂ NRs and 4 mg of N-KB were firstly dispersed in 950 μ L anhydrous ethanol by ultrasonication for 20 min. Then 50 μ L of Nafion solution (5 wt. %) was added into α -MnO₂ NRs/N-KB dispersion and continuously ultrasonicated for 20 min to get a homogeneous catalytic ink. Catalytic inks of 20 wt. % Pt/C and IrO₂/N-KB were also prepared to fabricate the standard catalysts for ORR and OER respectively. 6 mg of commercial 20 wt. % Pt/C (Johnson Matthey) were used to fabricate the Pt/C catalytic ink with the similar method. The preparations of KB, N-KB and pure α -MnO₂ catalytic inks are all the same with the Pt/C. Catalytic inks of IrO₂/N-KB contains 2 mg IrO₂ and 4 mg N-KB. Finally, 8 μ L of as-prepared catalytic ink were loaded onto the surface of glassy carbon disk electrode to obtain a mass loading of 0.2446 mg cm⁻².

Prior to the electrochemical tests, high-purity O₂ was purged in the electrolyte for 30 min. The LSV was measured from 0.2 to −1.0 V (vs. Ag/AgCl) at a scan rate of 10 mV·s^{−1} with a rotation rate of 1600 rpm. The cyclic voltammetry (CV) was measured at a scan rate of 100 mV·s^{−1}. OER LSV measurements were carried out at a scan rate of 10 mV·s^{−1} at the potential window of 0.2–1.0 V (vs. Ag/AgCl). The EIS were scanned in the frequency range of 10⁵–0.1 Hz at −0.2 V or 0.7 V (vs. Ag/AgCl) with the amplitude of 5 mV in O₂-saturated 0.1 M KOH solution [12,21,22].

All potentials were finally converted to the values versus reversible hydrogen electrode (RHE) according to the Nernst equation given in Equation (1).

$$E_{RHE} = E_{Ag/AgCl} + 0.059pH + E_{Ag/AgCl}^0 \quad (1)$$

where E_{RHE} is the applied potential vs. RHE; $E_{Ag/AgCl}$ represents the applied potential versus Ag/AgCl reference electrode and $E_{Ag/AgCl}^0$ (0.2046 V at 25 °C) is the standard electrode potential of the Ag/AgCl electrode.

The number of electron transferred (n) was estimated according to the Koutecky-Levich equation given as follows [39,41,42]:

$$\frac{1}{j} = \frac{1}{j_L} + \frac{1}{j_K} = \frac{1}{B\omega^{1/2}} + \frac{1}{j_K} \quad (2)$$

$$B = 0.62nFC_0D_0^{2/3}\nu^{-1/6} \quad (3)$$

The kinetic current density (j_K) for Tafel plots was determined according to the following equation: [34]

$$j_K = \frac{j_L \times j}{j_L - j} \quad (4)$$

where j , j_L and j_K are the recorded current density, the diffusion-limiting and kinetic current density, respectively. ω is the electrode rotating rates (rad·s^{−1}), n means the transferred electron number, F is the Faraday constant (96,485 C·mol^{−1}). C_0 (1.2 × 10^{−3} mol·L^{−1}) and D_0 (1.9 × 10^{−5} cm²·s^{−1}) correspond to the bulk concentration and diffusion coefficient of O₂ in 0.1 mol·L^{−1}, respectively. The ν represents the kinematic viscosity of the electrolyte (0.01 cm²·s^{−1}).

To further reveal the ORR mechanism, the peroxide yields (H₂O₂%) and the electron transfer number were calculated, respectively, using Equations (5) and (6) as follows [34]:

$$\text{H}_2\text{O}_2 (\%) = 200 \times \frac{I_r/N}{I_d + I_r/N} \quad (5)$$

$$n = 4 \times \frac{I_d}{I_d + I_r/N} \quad (6)$$

where I_d , I_r and N are the disk current, ring current and the collection efficiency, respectively. The empirical collection efficiency of Pt ring in RRDE experiments was 0.37 using [Fe(CN)₆]^{3−/4−} couple [34,42].

4. Conclusions

In this work, two α -MnO₂ nanorod samples were prepared from the oxidation of a MnSO₄ precursor by KMnO₄ under various hydrothermal reaction temperatures and time. Then, nanorod-like α -MnO₂ composited with N-doped ketjenblack carbon is obtained as electrocatalyst for ORR and OER. The MnO₂-150-0.5 sample shows smaller sizes than that of MnO₂-120-12 samples. Moreover, the higher ratio of Mn³⁺/Mn⁴⁺ for MnO₂-150-0.5 samples are confirmed by Mn 2p XPS spectra and Mn³⁺/Mn⁴⁺ redox peaks in CV curves. As a result, MnO₂-150-0.5/N-KB displays the superior ORR catalytic activity, with much more positive half-wave potential and much higher limiting current density (0.76 V and 6.0 mA·cm^{−2}), comparable to that of Pt/C (0.82 V and 5.10 mA·cm^{−2} respectively). MnO₂-150-0.5/N-KB also shows high electron transfer number and low peroxide yield during the

ORR process in the whole potential range of 0–1.0 V. The OER activities of these two samples were also compared. The MnO₂-150-0.5/N-KB exhibits better OER activity with low overpotential and charge transfer resistance, comparable to IrO₂/N-KB. All the results confirm that the smaller size, higher amount of Mn³⁺ and low charge transfer resistance favors for ORR and OER. To conclude, MnO₂-150-0.5/N-KB shows outstanding merit such as low cost, high efficient, facile fabrication and is expected to apply in alkaline fuel cells and metal/air batteries as a promising alternative catalyst. This report offers a new strategy for scalable preparation of more efficient and cost-effective α -MnO₂ for ORR and OER catalysts by easily regulated hydrothermal method.

Acknowledgments: This work was financially supported by the National Nature Science Foundation of China (Grant No. 61703152), Hunan Provincial Natural Science Foundation (2018JJ3134) and Zhuzhou Science and Technology Plans (201707201806), the Undergraduates Innovation Funds of Hunan University of Technology (HUT2018), and the Undergraduates Innovation Funds of College of Life Science and Chemistry (CLSC2018).

Author Contributions: Guangli Li and Fuzhi Li conceived and designed the experiments; Mei Wang and Kui Chen performed the experiments; Jun Liu, Quanguo He, Guangli Li and Fuzhi Li analyzed the data; Mei Wang, Kui Chen, Jun Liu, Quanguo He, Guangli Li and Fuzhi Li contributed reagents/materials/analysis tools; Guangli Li and Fuzhi Li wrote the paper.

Conflicts of Interest: The authors declare no conflict of interest.

References

1. Yang, S.; Wang, Z.; Cao, Z.; Mao, X.; Shi, M.; Li, Y.; Zhang, R.; Yin, Y. Facile synthesis of well dispersed spinel cobalt manganese oxides microsphere as efficient bi-functional electrocatalysts for oxygen reduction reaction and oxygen evolution reaction. *J. Alloys Compd.* **2017**, *721*, 482–491. [[CrossRef](#)]
2. Xue, Y.; Miao, H.; Sun, S.; Wang, Q.; Li, S.; Liu, Z. (La_{1-x} Sr_x)_{0.98}MnO₃ perovskite with a-site deficiencies toward oxygen reduction reaction in aluminum-air batteries. *J. Power Sources* **2017**, *342*, 192–201. [[CrossRef](#)]
3. Chen, L.; Cui, X.; Wang, Y.; Wang, M.; Qiu, R.; Shu, L.; Hua, Z.; Cui, F.; Wei, C.; Shi, J. One-step synthesis of sulfur doped graphene foam for oxygen reduction reactions. *Dalton Trans.* **2014**, *43*, 3420–3423. [[CrossRef](#)] [[PubMed](#)]
4. Patel, P.P.; Datta, M.K.; Velikokhatnyi, O.I.; Kuruba, R.; Damodaran, K.; Jampani, P.; Gattu, B.; Shanthi, P.M.; Damle, S.S.; Kumta, P.N. Noble metal-free bifunctional oxygen evolution and oxygen reduction acidic media electro-catalysts. *Sci. Rep.* **2016**, *6*, 28367. [[CrossRef](#)] [[PubMed](#)]
5. Sakaushi, K.; Fellingner, T.P.; Antonietti, M. Bifunctional metal-free catalysis of mesoporous noble carbons for oxygen reduction and evolution reactions. *ChemSuschem* **2015**, *8*, 1156–1160. [[CrossRef](#)] [[PubMed](#)]
6. Sa, Y.J.; Kwon, K.; Cheon, J.Y.; Kleitz, F.; Sang, H.J. Ordered mesoporous Co₃O₄ spinels as stable, bifunctional, noble metal-free oxygen electrocatalysts. *J. Mater. Chem.* **2013**, *1*, 9992–10001. [[CrossRef](#)]
7. Lübke, M.; Sumboja, A.; Mccafferty, L.; Armer, C.F.; Handoko, A.D.; Du, Y.; Mccoll, K.; Cora, F.; Brett, D.; Liu, Z. Transition-metal-doped α -MnO₂ nanorods as bifunctional catalysts for efficient oxygen reduction and evolution reactions. *Chemistryselect* **2018**, *3*, 2613–2622. [[CrossRef](#)]
8. Gu, W.; Hu, L.; Li, J.; Wang, E. Recent advancements in transition metal-nitrogen-carbon catalysts for oxygen reduction reaction. *Electroanalysis* **2018**, *30*, 1–13. [[CrossRef](#)]
9. Wang, Y.; Liu, Q.; Hu, T.; Zhang, L.; Deng, Y. Carbon supported MnO₂-CoFe₂O₄ with enhanced electrocatalytic activity for oxygen reduction and oxygen evolution. *Appl. Surf. Sci.* **2017**, *403*, 51–56. [[CrossRef](#)]
10. Ghosh, S.; Kar, P.; Bhandary, N.; Basu, S.; Maiyalagan, T.; Sardar, S.; Pal, S.K. Reduced graphene oxide supported hierarchical flower like manganese oxide as efficient electrocatalysts toward reduction and evolution of oxygen. *Int. J. Hydrogen Energy* **2017**, *42*, 4111–4122. [[CrossRef](#)]
11. Wu, X.; Gao, X.; Xu, L.; Huang, T.; Yu, J.; Wen, C.; Chen, Z.; Han, J. Mn₂O₃ doping induced the improvement of catalytic performance for oxygen reduction of MnO. *Int. J. Hydrogen Energy* **2016**, *41*, 16087–16093. [[CrossRef](#)]
12. Wei, Z.H.; Zhao, T.S.; Zhu, X.B.; Tan, P. MnO_{2-x} nanosheets on stainless steel felt as a carbon- and binder-free cathode for non-aqueous lithium-oxygen batteries. *J. Power Sources* **2016**, *306*, 724–732. [[CrossRef](#)]

13. Sumboja, A.; Ge, X.; Zheng, G.; Goh, F.W.T.; Hor, T.S.A.; Zong, Y.; Liu, Z. Durable rechargeable zinc-air batteries with neutral electrolyte and manganese oxide catalyst. *J. Power Sources* **2016**, *332*, 330–336. [[CrossRef](#)]
14. Pargoletti, E.; Cappelletti, G.; Minguzzi, A.; Rondinini, S.; Leoni, M.; Marelli, M.; Vertova, A. High-performance of bare and Ti-doped α -MnO₂ nanoparticles in catalyzing the oxygen reduction reaction. *J. Power Sources* **2016**, *325*, 116–128. [[CrossRef](#)]
15. Cheng, F.; Su, Y.; Liang, J.; Tao, Z.; Chen, J. MnO₂-based nanostructures as catalysts for electrochemical oxygen reduction in alkaline media. *Chem. Mater.* **2010**, *22*, 898–905. [[CrossRef](#)]
16. Meng, Y.; Song, W.; Huang, H.; Ren, Z.; Chen, S.Y.; Suib, S.L. Structure-property relationship of bifunctional MnO₂ nanostructures: Highly efficient, ultra-stable electrochemical water oxidation and oxygen reduction reaction catalysts identified in alkaline media. *J. Am. Chem. Soc.* **2014**, *136*, 11452–11464. [[CrossRef](#)] [[PubMed](#)]
17. Stoerzinger, K.A.; Risch, M.; Han, B.; Yang, S.H. Recent insights into manganese oxides in catalyzing oxygen reduction kinetics. *ACS Catal.* **2015**, *5*, 446–449. [[CrossRef](#)]
18. Najafpour, M.M.; Renger, G.; Holyńska, M.; Moghaddam, A.N.; Aro, E.M.; Carpentier, R.; Nishihara, H.; Eatonrye, J.J.; Shen, J.R.; Allakhverdiev, S.I. Manganese compounds as water-oxidizing catalysts: From the natural water-oxidizing complex to nanosized manganese oxide structures. *Chem. Rev.* **2016**, *116*, 2886. [[CrossRef](#)] [[PubMed](#)]
19. Han, G.Q.; Liu, Y.R.; Hu, W.H.; Dong, B.; Li, X.; Shang, X.; Chai, Y.M.; Liu, Y.Q.; Liu, C.G. Crystallographic structure and morphology transformation of MnO₂ nanorods as efficient electrocatalysts for oxygen evolution reaction. *J. Electrochem. Soc.* **2016**, *163*, H67–H73. [[CrossRef](#)]
20. Pokhrel, R.; Goetz, M.K.; Shaner, S.E.; Wu, X.; Stahl, S.S. The “best catalyst” for water oxidation depends on the oxidation method employed: A case study of manganese oxides. *J. Am. Chem. Soc.* **2015**, *137*, 8384–8387. [[CrossRef](#)] [[PubMed](#)]
21. Liang, S.; Teng, F.; Bulgan, G.; Ruilong Zong, A.; Zhu, Y. Effect of phase structure of MnO₂ nanorod catalyst on the activity for CO oxidation. *J. Phys. Chem. C* **2008**, *112*, 5307–5315. [[CrossRef](#)]
22. Cao, Y.L.; Yang, H.X.; Ai, X.P.; Xiao, L.F. The mechanism of oxygen reduction on MnO₂-catalyzed air cathode in alkaline solution. *J. Electroanal. Chem.* **2003**, *557*, 127–134. [[CrossRef](#)]
23. Ma, Y.; Wang, R.; Wang, H.; Key, J.; Ji, S. Control of MnO₂ nanocrystal shape from tremella to nanobelt for enhancement of the oxygen reduction reaction activity. *J. Power Sources* **2015**, *280*, 526–532. [[CrossRef](#)]
24. Xiao, W.; Wang, D.; Lou, X.W. Shape-controlled synthesis of MnO₂ nanostructures with enhanced electrocatalytic activity for oxygen reduction. *J. Phys. Chem. C* **2010**, *114*, 1430–1434. [[CrossRef](#)]
25. Suntivich, J.; Gasteiger, H.A.; Yabuuchi, N.; Nakanishi, H.; Goodenough, J.B.; Shao-Horn, Y. Design principles for oxygen-reduction activity on perovskite oxide catalysts for fuel cells and metal-air batteries. *Nat. Chem.* **2011**, *3*, 647. [[CrossRef](#)]
26. Suntivich, J.; May, K.J.; Gasteiger, H.A.; Goodenough, J.B.; Shaohorn, Y. A perovskite oxide optimized for oxygen evolution catalysis from molecular orbital principles. *Science* **2012**, *43*, 1383–1385. [[CrossRef](#)] [[PubMed](#)]
27. Cheng, F.; Zhang, T.; Zhang, Y.; Du, J.; Han, X.; Chen, J. Enhancing electrocatalytic oxygen reduction on MnO₂ with vacancies. *Angew. Chem. Int. Ed.* **2013**, *52*, 2474. [[CrossRef](#)] [[PubMed](#)]
28. Zhang, T.; Cheng, F.; Du, J.; Hu, Y.; Chen, J. Efficiently enhancing oxygen reduction electrocatalytic activity of MnO₂ using facile hydrogenation. *Adv. Energy Mater.* **2015**, *5*, 1400654. [[CrossRef](#)]
29. Davis, D.J.; Lambert, T.N.; Vigil, J.A.; Rodriguez, M.A.; Brumbach, M.T.; Coker, E.N.; Limmer, S.J. Role of Cu-ion doping in Cu- α -MnO₂ nanowire electrocatalysts for the oxygen reduction reaction. *J. Phys. Chem. C* **2014**, *118*, 17342–17350. [[CrossRef](#)]
30. King’Ondu, C.K.; Opembe, N.; Chen, C.H.; Ngala, K.; Huang, H.; Iyer, A.; Garcés, H.F.; Suib, S.L. Manganese oxide octahedral molecular sieves (OMS-2) multiple framework substitutions: A new route to OMS-2 particle size and morphology control. *Adv. Funct. Mater.* **2011**, *21*, 312–323. [[CrossRef](#)]
31. Chen, S.Y.; Song, W.; Lin, H.J.; Wang, S.; Biswas, S.; Mollahosseini, M.; Kuo, C.H.; Gao, P.X.; Suib, S.L. Manganese oxide nanoarray-based monolithic catalysts: Tunable morphology and high efficiency for CO oxidation. *ACS Appl. Mater. Interfaces* **2016**, *8*, 7834. [[CrossRef](#)] [[PubMed](#)]
32. Zheng, X.; Yu, L.; Lan, B.; Cheng, G.; Lin, T.; He, B.; Ye, W.; Sun, M.; Ye, F. Three-dimensional radial α -MnO₂ synthesized from different redox potential for bifunctional oxygen electrocatalytic activities. *J. Power Sources* **2017**, *362*, 332–341. [[CrossRef](#)]

33. Ozcan, S.; Tokur, M.; Cetinkaya, T.; Guler, A.; Uysal, M.; Guler, M.O.; Akbulut, H. Free standing flexible graphene oxide + α -MnO₂ composite cathodes for Li-air batteries. *Solid State Ion.* **2016**, *286*, 34–39. [[CrossRef](#)]
34. Li, F.; Fu, L.; Li, J.; Yan, J.; Tang, Y.; Pan, Y.; Wangz, H. Ag/Fe₃O₄-N-doped ketjenblack carbon composite as highly efficient oxygen reduction catalyst in Al-air batteries. *J. Electrochem. Soc.* **2017**, *164*, A3595–A3601. [[CrossRef](#)]
35. Li, J.; Ren, Y.; Wang, S.; Ren, Z.; Yu, J. Transition metal doped MnO₂ nanosheets grown on internal surface of macroporous carbon for supercapacitors and oxygen reduction reaction electrocatalysts. *Appl. Mater. Today* **2016**, *3*, 63–72. [[CrossRef](#)]
36. Zhang, Q.; Cheng, X.; Feng, X.; Qiu, G.; Tan, W.; Liu, F. Large-scale size-controlled synthesis of cryptomelane-type manganese oxide OMS-2 in lateral and longitudinal directions. *J. Mater. Chem. A* **2011**, *21*, 462–465. [[CrossRef](#)]
37. Lee, S.; Nam, G.; Sun, J.; Lee, J.S.; Lee, H.W.; Chen, W.; Cho, J.; Cui, Y. Enhanced intrinsic catalytic activity of λ -MnO₂ by electrochemical tuning and oxygen vacancy generation. *Angew. Chem. Int. Ed.* **2016**, *128*, 8599–8604. [[CrossRef](#)] [[PubMed](#)]
38. Brenet, J.P. Electrochemical behaviour of metallic oxides. *J. Power Sources* **1979**, *4*, 183–190. [[CrossRef](#)]
39. Li, J.; Zhou, Z.; Liu, K.; Li, F.; Peng, Z.; Tang, Y.; Wang, H. Co₃O₄/Co-N-C modified ketjenblack carbon as an advanced electrocatalyst for Al-air batteries. *J. Power Sources* **2017**, *343*, 30–38. [[CrossRef](#)]
40. Liu, K.; Huang, X.; Wang, H.; Li, F.; Tang, Y.; Li, J.; Shao, M. Co₃O₄-CeO₂/C as a highly active electrocatalyst for oxygen reduction reaction in Al-air batteries. *ACS Appl. Mater. Int.* **2016**, *8*, 34422–34430. [[CrossRef](#)] [[PubMed](#)]
41. Liu, K.; Peng, Z.; Wang, H.; Ren, Y.; Liu, D.; Li, J.; Tang, Y.; Zhang, N. Fe₃C@Fe/N doped graphene-like carbon sheets as a highly efficient catalyst in Al-air batteries. *J. Electrochem. Soc.* **2017**, *164*, F475–F483. [[CrossRef](#)]
42. Li, J.; Chen, J.; Wang, H.; Ren, Y.; Liu, K.; Tang, Y.; Shao, M. Fe/N co-doped carbon materials with controllable structure as highly efficient electrocatalysts for oxygen reduction reaction in Al-air batteries. *Energy Storage Mater.* **2017**, *8*, 49–58. [[CrossRef](#)]



© 2018 by the authors. Licensee MDPI, Basel, Switzerland. This article is an open access article distributed under the terms and conditions of the Creative Commons Attribution (CC BY) license (<http://creativecommons.org/licenses/by/4.0/>).